Observation of Orbital Angular Momentum Transfer from Bessel-shaped Acoustic Vortices to Diphasic Liquid-Microparticle Mixtures

ZhenYu Hong,[1,2,*] Jie Zhang,[2] and Bruce W. Drinkwater[2,†]

[1]Department of Applied Physics, Northwestern Polytechnical University, Xi'an 710072, China

[2]Department of Mechanical Engineering, University Walk, University of Bristol, Bristol BS8 1TR, UK

We observe distinct regimes of orbital angular momentum (OAM) transfer from two-dimensional Bessel-shaped acoustic vortices to matter. In a homogeneous diphasic mixture of microparticles and water, slow swirling about the vortex axis is seen. This effect is driven by absorption of OAM across the mixture, the motion following the OAM density distribution. Larger particles are formed into clusters by the acoustic radiation force making the mixture non-homogeneous. Here OAM transfer to the microparticle clusters dominates and they spin at high speeds entraining the surrounding fluid.

Keywords:

Orbital angular momentum, acoustic vortices, acoustic radiation force, rotational motion

PACS numbers: 43.25.Nm, 43.25.Qp, 47.15.G-

[*]hongzy@nwpu.edu.cn

[†]b.drinkwater@bristol.ac.uk

Introduction. -Acoustic waves with screw dislocations at their wavefronts, or acoustic vortices, were first observed and theoretically studied by Nye and Berry [1]. They are characterized by an azimuthal, θ, phase dependence of $e^{-im\theta}$. Here the integer m is called the topological charge or the order of the helicoidal beam and encodes the angular rotation rate of the wavefront. Vortices have since been shown to be an intrinsic property of all waves. For example, in optics, He *et al* [2] observed the orbital angular momentum (OAM) transfer from a laser beam with a helical wavefront to absorptive particles. A significant research effort has now demonstrated the transfer of optical OAM to a range of particles and vortex topologies [3-9]. Emerging applications include optical tweezers [10] and communications [11,12].

Acoustic helicoidal fields can be generated by various means, e.g., using an acoustic source with a helicoidal radiating surface [13]; an array of individually addressed sources excited with appropriate phases [14] or via the optoacoustic technique [15]. Sparsely distributed pizeoelectic sources have been used to generate acoustic helicoidal fields and, with a large (relative to the wavelength) absorptive disk, directly observe OAM transfer to a macroscopic object [16,17]. Demore *et al*, used an ultrasonic array with 1000 addressable sources and a large absorptive disc to demonstrate that the ratio between angular momentum flux and acoustic power is equal to the ratio of the topological charge of an acoustic helicoidal beam and its angular frequency [18]. Thomas and Marchiano [19], generalized this relation to the weakly non-linear regime and experimentally validated their model [19,20]. Recently, Anhauser *et al* quantitatively analysed the balance between the OAM-driven torque exerted by an acoustic helicoidal beam on a large absorptive disk and the viscous retarding torque exerted by the host fluid [21]. They separated the effects of rotation due to absorption of OAM by the disc and drag from an effect they called *rotational acoustic streaming*. In doing so they made the first observation of fluid rotation driven by an acoustic vortex. In parallel, the propagation of acoustic helicoidal beams and their interaction with objects has been explored from a theoretical perspective [22-24]. In particular Riaud *et al* [25] described a model based on an extension of Eckart perturbation theory which predicts the above rotational acoustic streaming phenomena due to a Bessel beam.

Inspired by optical tweezers, acoustic radiation force (ARF) trapping devices for manipulating microscopic objects have attracted significant attention, particularly for cell manipulation applications [26,27]. Note that the ARF involves the transfer of linear momentum to objects. There are two approaches to achieving acoustic trapping; the first uses a wavelength smaller than the particle and trapping occurs at the focus of a propagating acoustic beam [28] whereas the second uses a wavelength greater than the particle size and trapping occurs in a standing wave field controlled by an array of sources [29-32]. Recently, an array-based standing-wave ARF trap device has been used to trap microparticles at the null in the centre of a first-order two-dimensional (2D) Bessel-shaped acoustic vortex [33]. Adjusting the phase of the array elements enabled the central vortex null to be moved and hence the microparticles to be manipulated. This also provides the possibility of manipulating the particle rotation in the resultant acoustic streaming fields.

In this Letter, we observe the transfer of the OAM of 2D Bessel-shaped acoustic vortices to fluids and a range of microscale matter. We also explore the influence of the ARF on the OAM transfer mechanics. Bessel-shaped vortices up to order 4 are experimentally realised using a 64-source standing-wave ARF trap device. This experiment allows us to make the first observations of the transfer of acoustic OAM to microparticles of size order 1-100 μm, which is significantly smaller than the acoustic wavelength (λ = 625 μm).

Experimental configuration. – Fig. 1 shows the apparatus which consists of 64 individually addressable piezoelectric sources arranged at a pitch of 0.54 mm around a ring (in the r-θ plane) with radius, $r_0 = 5.49$ mm. The inner surface of the sources is coated with a quarter-wavelength matching layer and the outer surface with an absorbing layer which together minimize the reflection of acoustic waves. Previous analysis [33] showed that at the device boundary, the normal incidence reflection coefficient, $R \approx 0.05$ and so the acoustic field can be calculated assuming free-field conditions. The central volume is filled with a diphasic mixture of liquid and microparticles and sealed top and bottom with glass coverslips to produce a cylindrical chamber, of 2 mm in height. The chamber was observed in the z-direction using a microscope (GX Optical ML3030, UK) and high speed video camera (Allied Vision Technologies 1394, Germany). After introduction of the mixture, streaming observations were

made within the first minute before any significant sedimentation had occurred. Due to the limited size of the chamber and the non-slip boundary condition imposed by enclosing coverslips, the acoustic streaming will vary in the *z*-direction. To minimise the effect of these boundary conditions the microscope was focused on the mid-section and had a depth of field of 40 μm.

In this device, a Bessel-shaped vortex, without propagation in the *z*-axis is generated using sinusoidal drive signals which are phase-shifted such that there is a ramp of $2m\pi$ phase delay around the array, i.e., the relative phase, ϕ_n, of the signal applied to each of the *N* sources, $n = 1, 2, 3, \ldots, N$ is,

$$\phi_n = \frac{2m\pi(n-1)}{N}. \tag{1}$$

This results in the generation of an approximately Bessel-shaped velocity potential given by [34],

$$\psi_m(r) = \psi_0 J_m(kr) e^{-im\theta}, \tag{2}$$

where, (r, θ) are the polar coordinates, ψ_0 is the amplitude, J_m is an m^{th}-order Bessel function and *k* is the wavenumber ($k = 2\pi f/c$, *f* is frequency and *c* is wave speed). The acoustic field in the device was measured using Schlieren photography and good agreement with Eq. (2) was seen [35]. The resulting time-averaged angular momentum density distribution is [36],

$$\overline{D}_m(r) = \frac{k\rho m}{2c} |\psi_m|^2, \tag{3}$$

where ρ is the density of host fluid.

Slow swirling of fluid. – Bessel-shaped vortices of $k = 1.0 \times 10^4$ m^{-1} are generated by driving the sources with sinusoidal voltages (V_{pp} = 25 V, *f* = 2.4 MHz) and phase delays chosen according to Eq. (1). A homogeneous diphasic mixture is created by adding a small quantity of 0.5-μm-radius spherical polystyrene microparticles (Bangs Laboratories Inc, USA, ρ_{PS} = 1062 kg/m^3 and c_{PS} = 2400 m/s) to water (ρ = 1000 kg/m^3, *c* = 1500 m/s). Here, $ka = 0.005$, where *a* is particle radius, and the ARF, which is proportional to a^3, is negligible [37]. For this reason the diphasic fluid maintains homogeneity and the small spheres become tracer particles. The motion of the particles, and hence the fluid, is extracted using Particle Image Velocimetry (PIV) [38].

Figures 2(a)-(d) show snapshots of the particles and fluid velocity vectors measured in the central region of Bessel-shaped vortices for m = 1-4 (supplementary materials in [39] show this swirling motion). Note that the radial component of the velocity vectors is small (maximum 20%, 16%, 15% and 12% difference from the average azimuthal component for m=1-4 respectively) and we attribute this to small differences in the source strength which lead to deviations from perfect Bessel shapes.

As shown in Fig. 1, the torque produced by OAM transfer from a Bessel-shaped vortex to an elemental ring of fluid, S_r, is, $d\Gamma^a(r) = \alpha \overline{D}_m(r) 2\pi r dr$, where α is a coefficient which governs OAM absorption by the fluid and is equivalent to the attenuation coefficient in Eq. (9) [21]. Hence, by integrating radially the driving torque is,

$$\Gamma^a(r) = \int_0^r 2\pi\alpha\, \overline{D}_m(r) r dr. \tag{4}$$

Considering Eq. (15.17) in [40] with zero radial velocity, the drag torque caused by the viscosity of fluid on the boundary of S_r is,

$$\Gamma^d(r) = -2\pi\eta r^3 \frac{d\omega}{dr}, \tag{5}$$

where η is dynamic viscosity of fluid and ω is the rotation rate of fluid. Once the rotation of the fluid stabilises, the OAM-driven torque and the retarding viscous drag on S_r are in equilibrium,

$$\omega(r) = mk\beta|\psi_0|^2 \int_{r_0}^{r} \frac{1}{x_2^3} \int_0^{x_2} J_m^2(kx_1) x_1 dx_1 dx_2, \tag{6}$$

where, $\beta = \alpha\rho/2\eta c$, which governs momentum transfer efficiency and $\omega(r_0) = 0$. Note that the above model is identical to the one developed in [21] which was written for torque rather than for force. By substituting $V_\phi = r\omega$ into Eq. (8) of [21], Eq. (6) in the present paper for a Bessel-shaped field is obtained.

Figures 2(e)-(h) show velocity vectors from Eq. (6) and the time-averaged angular momentum density from Eq. (3). Figures 2(i)-(l) show excellent agreement between the measured (averaged circumferentially) and predicted rotation rates suggesting that Eqs. (4)-(6) capture the governing physics. The constant $\beta|\psi_0|^2$ was determined by a least squares fit of Eq. (6) to the measured rotation data. Figs. 2(i)-(l) show a central region of approximately constant rotational speed which grows with Bessel order, following the time-averaged angular momentum density in Eq. (3). Beyond this central

region, the rotational rate decreases rapidly with r. These predicted rotational speed distributions are in qualitative agreement with the extended model presented in [25].

High speed spinning of flour microparticle clusters. – Somewhat larger microparticles, or those with greater acoustic contrast, are forced by ARF effects to locations which minimise acoustic potential energy. We use household flour particles of $1 < a < 10$ μm [41] and water to create this alternative OAM transfer regime. The ARF on these larger particles causes the diphasic particle-liquid mixture to become non-homogeneous: the flour microparticles move to acoustic energy minima forming clusters. From Fig. 3(a), for a first-order Bessel-shaped field, this results in a central cluster of microparticles and concentric rings corresponding to the zeros in this function. The central cluster, $r \leq 62$ μm spins at high speeds about the vortex axis (see supplementary materials in [39]). In this new regime $0.01 < ka < 0.1$ for the microparticles and $ka = 0.6$ for the cluster. The rotation rates at r = 62 μm were measured by monitoring the feature points, e.g., cluster edges, in consecutively captured images. The rotation rate of the cluster increases almost linearly with V_{pp}^2 and rises to 150 rad/s which is ~50 times that measured for a = 0.5-μm polystyrene particles in water (i.e. Fig. 2). We believe that the ARF driven clustering here forms a highly absorbing micro-target that leads to dramatically increased local absorption of OAM. Note that the cluster shown in the Fig. 3(a) spans the ring of high OAM density shown in Fig. 2(e) (i.e. r = 50-350 μm). In this regime, the low-speed rotation due to direct OAM transfer to the water near the cluster (< 4 rad/s at V_{pp} = 25 V from Fig. 2(i)) and associated drag, is negligible.

In a qualitative model of the flow of a Newtonian liquid between two rotating cylinders at low Reynolds numbers [40], the rotation rate between these cylinders is [21,40],

$$\frac{d^2\omega}{dr^2} + \frac{3}{r}\frac{d\omega}{dr} = 0. \tag{7}$$

Using the rotation measured at the cluster edge, r_1 = 62 μm, and $\omega(r_0) = 0$, the rotation rates at intermediate positions are predicted and shown in Fig. 3(c). Also shown in Fig. 3(c) are measurements at r_2 = 223 μm which agree well with this prediction. This strongly suggests that the rotation of the

water is driven by the spinning of the centrally trapped cluster and is only indirectly linked to OAM transfer.

According to the above qualitative flow model, the driving torque of the inner cylindrical surface at r_1 = 62 μm is [40],

$$\Gamma^a(r_1) = \frac{4\pi\eta r_0^2 r_1^2}{r_0^2 - r_1^2}\omega(r_1). \quad (8)$$

This indicates $\Gamma^a \propto \omega$ and from Fig. 3(b) $\Gamma^a \propto V_{\mathrm{pp}}^2$. Assuming that the piezoelectric sources behave linearly, the acoustic power is linearly related to the square of voltage, i.e., $P \propto V_{\mathrm{pp}}^2$ [42] and hence $\Gamma^a \propto P$. Therefore, assuming that the torque originates from OAM transfer, this observation suggests that the ratio of OAM flux to acoustic power is also linear, in agreement with theoretical predictions of Zhang and Marston [43].

Positional locking of silica microparticles. – As the acoustic contrast increases further, microparticles become locked in place more strongly by the ARF. Here we observe that 1-μm-radius silica microparticles (Bang Laboratories ltd, ρ_S = 1800 kg/m^3 and c_S = 5968 m/s) rotate slowly and sporadically around the vortex axis in patterns dictated by the ARF (see supplementary materials in [39]). Figure 4(a) shows the distribution of silica microparticles and the orbital trajectories followed. Figure 4(b) shows that the rotation rates of particles measured by PIV in Orbits 1 and 2 are slow and vary circumferentially. We believe that small differences in the source output leads to small experimental differences from a perfect Bessel-shaped field. This non-axisymmetrical ARF then causes weak acoustic traps to form in certain circumferential locations, inhibiting rotational motion due to OAM absorption.

In conclusion, the transfer of OAM from 2D Bessel-shaped acoustic vortices to diphasic liquid-microparticle mixtures is governed by the relative contribution of the ARF and OAM. The ARF is governed by the size of the particles and acoustic contrast between the particles and surrounding liquid whereas their ability to absorb OAM is governed by the local attenuation coefficient. In the presence of an acoustic vortex, small (or low contrast) particles swirl with the fluid due to OAM; larger (or higher contrast) particles form into clusters due to ARF effects making the diphasic mixture non-homogeneous.

The central cluster rotates at high speed due to high OAM absorption by the cluster, entraining the surrounding fluid; still larger (or yet higher contrast) particles are locked in position within the non-homogeneous mixture by any non-axisymmetric ARF components and rotate non-uniformly and slowly due to OAM absorption. The observations reveal that a linear relationship between rotational speed and acoustic power holds true for microparticles in vortices (i.e. $ka < 1$), as it does for macroscale objects. This work has applications in harnessing acoustic vortices for manipulation of objects such as microparticles and control of their rotation in microfluidic devices and ARF trap devices. The phenomena observed are expected to be seen in similar 3D vortex fields.

This work was supported by China Scholarship Council, National Natural Science Foundation of China (Grant Nos. 51327901 and 11104223), Fundamental Research Funds for the Central Universities and Pump Priming Grant from University of Bristol. We are grateful to B. Wei for his support and M. Caleap for his experimental assistance.

REFERENCES

[1] J. F. Nye and M. V. Berry, Proc. R. Soc. A **336**, 165 (1974).

[2] H. He, M. E. J. Friese, N. R. Heckenberg, and H. Rubinsztein-Dunlop, Phys. Rev. Lett. **75**, 826 (1995).

[3] M. E. J. Friese, J. Enger, H. Rubinsztein-Dunlop, and N. R. Heckenberg, Phys. Rev. A **54**, 1593 (1996).

[4] N. B. Simpson, K. Dholakia, L. Allen, and M. J. Padgett, Opt. Lett. **22**, 52 (1997).

[5] A. T. O'Neil and M. J. Padgett, Opt. Commun. **185**, 139 (2000).

[6] K. Volke-Sepulveda, V. Garces-Chavez, S. Chavez-Cerda, J. Arlt, and K. Dholakia, J. Opt. B **4**, S82 (2002).

[7] V. Garces-Chavez, D. McGloin, M. J. Padgett, W. Dultz, H. Schmitzer, and K. Dholakia, Phys. Rev. Lett. **91**, 093602 (2003).

[8] M. Dienerowitz and K. Dholakia, Topologica **2**, 008 (2009).

[9] V. N. Belyi, N. A. Khilo, S. N. kurilkina, and N. S. Kazak, J. Appl. Spectrosc. **80**, 458 (2013).

[10] S. Franke-Arnold, L. Allen, and M. Padgett, Laser Photon. Rev. **2**, 299 (2008).

[11] X. Cai, J. Wang, M. J. Strain, B. Johnson-Morris, J. Zhu, M. Sorel, J. L. O'Brien, M. G. Thompson, S. Yu, Science **338**, 363 (2012).

[12] N. Bozinovic, Y. Yang, Y. Ren, M. Tur, P. Kristensen, H. Huang, A. E. Willner, and S. Ramachandran, Science **340**, 1545 (2013).

[13] B. T. Hefner and P. L. Marston, J. Acoust. Soc. Am. **103**, 2971 (1998).

[14] B. T. Hefner and P. L. Marston, J. Acoust. Soc. Am. **106**, 3313 (1999).

[15] S. Gspan, A. Meyer, S. Bernet, and M. Ritsch-Marte, J. Acoust. Soc. Am. **115**, 1142 (2004).

[16] K. Volke-Sepulveda, A. O. Santillan, and R. R. Boullosa, Phys. Rev. Lett. **100**, 024302 (2008).

[17] K. D. Skeldon, C. Wilson, M. Edgar, and M. J. Padgett, New J. Phys. **10**, 013018 (2008).

[18] C. E. M. Demore, Z. Y. Yang, A. Volovick, S. Cochran, M. P. MacDonald, and G. C. Spalding, Phys. Rev. Lett. **108**, 194301 (2012).

[19] J.-L. Thomas and R. Marchiano, Phys. Rev. Lett. **91**, 244302 (2003).

[20] J.-L. Thomas, T. Brunet and F. Coulouvrat, Phys. Rev. E. **81**, 016601 (2010).

[21] A. Anhauser, R. Wunenburger, and E. Brasselet, Phys. Rev. Lett. **109**, 034301 (2012).

[22] D. Baresch, J.-L. Thomas, and R. Marchiano, J. Acoust. Soc. Am. **133**, 25 (2013).

[23] G. T. Silva, J. Acoust. Soc. Am. **136**, 2405 (2014).

[24] L. K. Zhang and P. L. Marston, J. Acoust. Soc. Am. **136**, 2917 (2014).

[25] A. Riaud, M. Baudoin, J.-L. Thomas, and O. B. Matar, Phys. Rev. E. **90**, 013008 (2014).

[26] J. Shi, D. Ahmed, X. Mao, S.-C. S. Lin, A. Lawit, and T. J. Huang, Lab Chip **9**, 2890 (2009).

[27] J. Friend and L. Y. Yeo, Rev. Mod. Phys. **83**, 647 (2011).

[28] J. Lee, C. Lee, H. H. Kim, A. Jakob, R. Lemor, S.-Y. Teh, A. Lee, and K. K. Shung, Biotechnol. Bioeng. **108**, 1643 (2011).

[29] D. Foresti, M. Nabavi, M. Klingauf, A. Ferrari, and D. Poulikakos, Pro. Natl. Acad. Sci. USA **110**, 12549 (2013).

[30] C. D. Wood, J. E. Cunningham, R. O'Rorke, C. Walti, E. H. Linfield, A. G. Davies, and S. D. Evans, Appl. Phys. Lett. **94**, 054101 (2009).

[31] C. R. P. Courtney, C. K. Ong, B. W. Drinkwater, A. L. Bernas-sau, P. D. Wilcox, and D. R. S. Cumming, Proc. R. Soc. A **468**, 337 (2012).

[32] L. Meng, F. Cai, J. Chen, L. Niu, Y. Li, J. Wu, and H. Zheng, Appl. Phys. Lett. **100**, 173701 (2012).

[33] C. R. P. Courtney, C. E. M. Demore, H. X. Wu, A. Grinenko, P. D. Wilcox, S. Cochran, and B. W. Drinkwater, Appl. Phys. Lett. **104**, 154103 (2014).

[34] B. A. Grinenko, P. D. Wilcox, C. R. P. Courtney, and B. W. Drinkwater, Proc. R. Soc. A **468**, 3571 (2012).

[35] A. Grinenko, M. P. MacDonald, C. R. P. Courtney, P. D. Wilcox, C. E. M. Demore, S. Cochran, and B. W. Drinkwater, Opt. Express **23**, 26 (2015).

[36] J. Lekner, J. Acoust. Soc. Am. **120**, 3475 (2006).

[37] J. Zhang, L. Meng, F. Cai, H. Zheng, and C. R. P. Courtney, Appl. Phys. Lett. **104**, 224103 (2014).

[38] W. Thielicke and E. J. Stamhuis, J. Open Research Software **2**, e30 (2014).

[39] See Supplementary Materials at [insert details]

[40] L. D. Landau and E. M. Lifshitz, *Fluid Mechanics*, Second English Edition, Translated from the Russian by J. B. Sykes and W. H. Reid , Pergamon Press, p. 48, 55, 56, 301 (1987).

[41] G. A. Hareland, J. Cereal Sci. **20**, 183 (1994).

[42] W. D. Shou, X. W. Huang, S. M. Duan, R. M. Xia, Z. L. Shi, X. M. Geng, F. Q. Li, Ultrasonics **44**, e17 (2006).

[43] L. K. Zhang and P. L. Marston, Phys. Rev. E **84**, 065601 (2011).

FIGURE CAPTIONS

FIG. 1. Schematic of the 64-source ARF trap device used to generate the acoustic vortices.

FIG. 2. Rotation of homogeneously distributed 0.5-μm-radius polystyrene microparticles in water in the presence of first to fourth order Bessel-shaped acoustic vortices. (a)-(d) Experimental velocity fields; (e)-(h) Predicted normalized orbital angular momentum density distributions and velocity fields; (i)-(l) Comparison of theoretically predicted and experimentally measured time-averaged rotation rates.

FIG. 3. High speed spin of the central cluster of flour microparticles in the presence of a first order Bessel-shaped acoustic vortex. (a) Cluster on the vortex axis and surrounding area with, r_1 = 62 μm and r_2 = 223 μm; (b) Rotation rates of the cluster trapped at $r < r_1$ as a function of the voltage, V_{pp}, applied to the piezoelectric sources; (c) Comparison of theoretical and experimental rotation rates at r_2 = 223 μm.

FIG. 4. Orbital motion of 1-μm-radius silica microparticles in the presence of a first-order Bessel-shaped acoustic vortex. (a) Photograph; (b) Rotation rates of microparticles in Orbits 1 and 2.

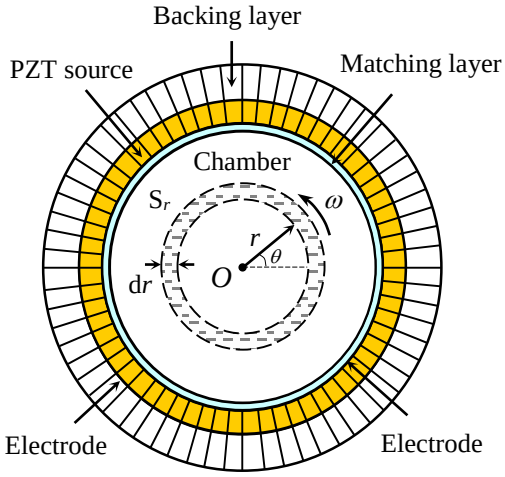
Backing layer
PZT source
Matching layer
Chamber
S_r
ω
r
θ
O
dr
Electrode
Electrode

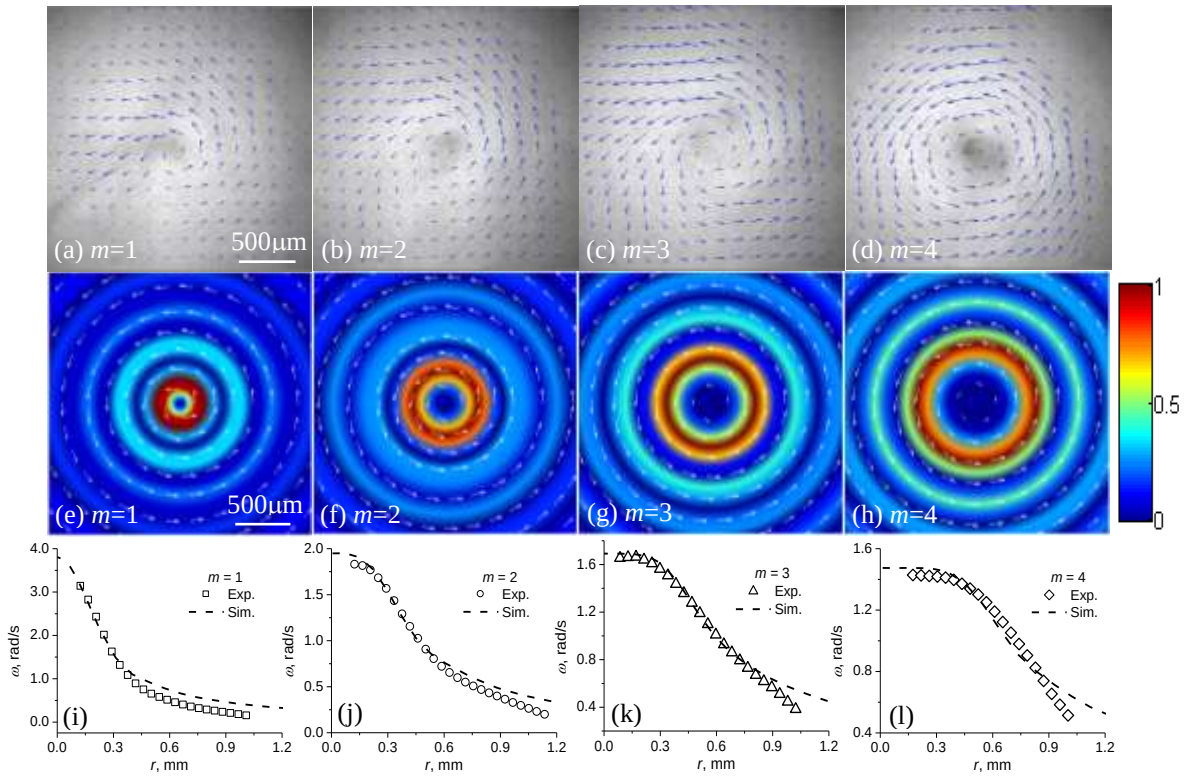
(a) m=1
500μm
(b) m=2
(c) m=3
(d) m=4
(e) m=1
500μm
(f) m=2
(g) m=3
(h) m=4
1
0.5
0
(i)
m = 1
Exp.
Sim.
ω, rad/s
r, mm
(j)
m = 2
Exp.
Sim.
ω, rad/s
r, mm
(k)
m = 3
Exp.
Sim.
ω, rad/s
r, mm
(l)
m = 4
Exp.
Sim.
ω, rad/s
r, mm

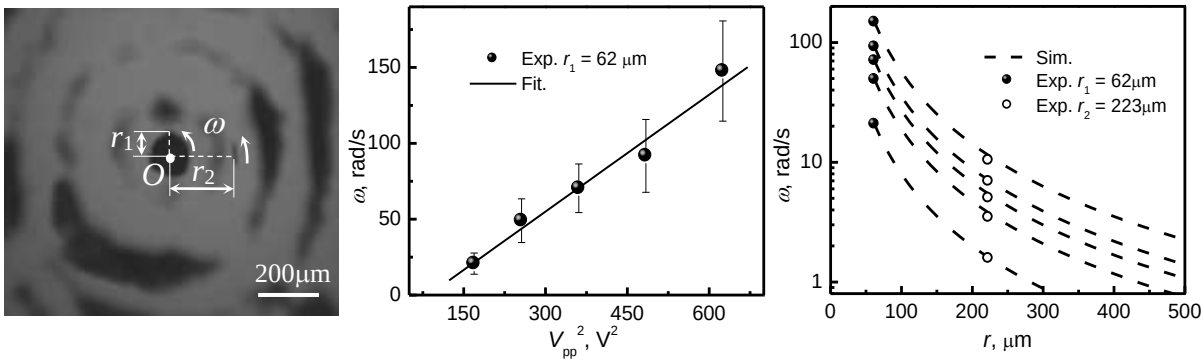
r_1
ω
O
r_2
200μm
Exp. r_1 = 62 μm
Fit.
ω, rad/s
V_{pp}^2, V^2
Sim.
Exp. r_1 = 62μm
Exp. r_2 = 223μm
r, μm

(a) (b) (c)

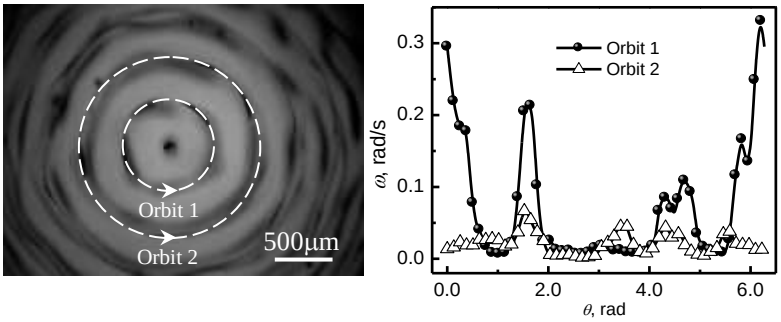
Orbit 1
Orbit 2
500μm
Orbit 1
Orbit 2
ω, rad/s
θ, rad
0.0
0.1
0.2
0.3
0.0
2.0
4.0
6.0

(a) (b)